MIT Libraries | DSpace@MIT

MIT Open Access Articles

Computationally Guided Intracerebral Drug Delivery via Chronically Implanted Microdevices

The MIT Faculty has made this article openly available. ***Please share*** how this access benefits you. Your story matters.

Citation: Ramadi, Khalil B. et al. "Computationally Guided Intracerebral Drug Delivery via Chronically Implanted Microdevices." Cell Reports, 31, 10 (June 2020): 107734 © 2020 The Author(s)

As Published: 10.1016/j.celrep.2020.107734

Publisher: Elsevier BV

Persistent URL: https://hdl.handle.net/1721.1/127209

Version: Final published version: final published article, as it appeared in a journal, conference proceedings, or other formally published context

Terms of use: Creative Commons Attribution-NonCommercial-NoDerivs License

Massachusetts Institute of Technology

Cell Reports

Computationally Guided Intracerebral Drug Delivery via Chronically Implanted Microdevices

Graphical Abstract

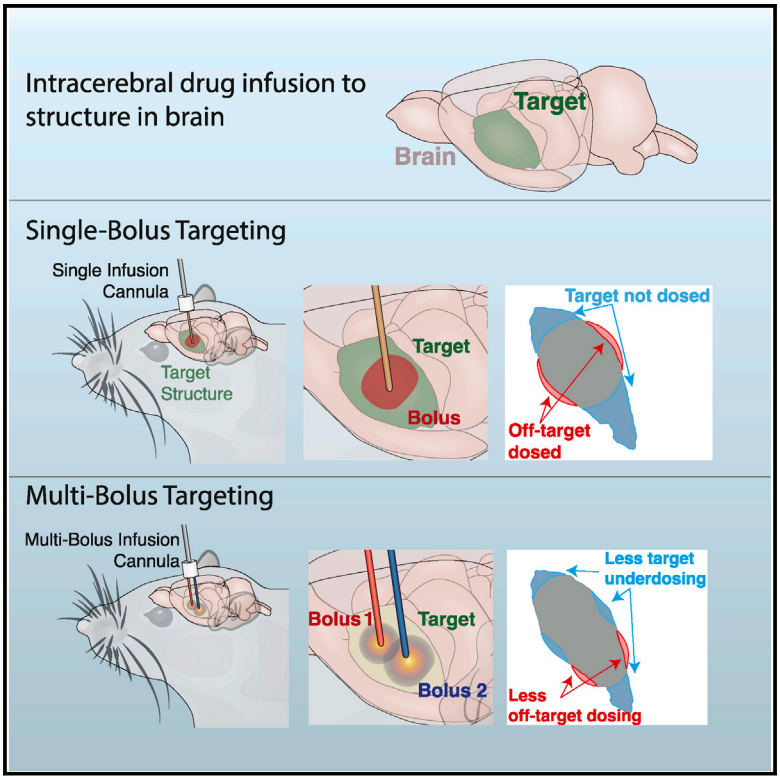

Highlights

- Multi-bolus targeting can improve coverage of irregularly shaped brain structures
- Volume and position of each bolus can be computed for a given infusate and target
- Rational fluidic design enables instantaneous delivery of multiple boluses
- Chronic neural probes replicate computational coverage estimates with 5% error

Authors

Khalil B. Ramadi, Ashvin Bashyam, Chris J. Frangieh, ..., Robert Langer, Ann M. Graybiel, Michael J. Cima

Correspondence

mjcima@mit.edu

In Brief

Ramadi et al. combine computational algorithms and rational fluidic design to develop a framework to maximize coverage of brain structures in intracerebral infusions while minimizing off-target leakage.

Ramadi et al., 2020, Cell Reports *31*, 107734
June 9, 2020 © 2020 The Author(s).
https://doi.org/10.1016/j.celrep.2020.107734

CellPress

Cell Reports

CellPress
OPEN ACCESS

Report

Computationally Guided Intracerebral Drug Delivery via Chronically Implanted Microdevices

Khalil B. Ramadi,[1,2,7] Ashvin Bashyam,[1,3,7] Chris J. Frangieh,[1,3] Erin B. Rousseau,[1,2] Max J. Cotler,[1,2] Robert Langer,[1,2,4] Ann M. Graybiel,[5] and Michael J. Cima[1,2,6,8,*]

[1]Koch Institute for Integrative Cancer Research, Massachusetts Institute of Technology, Cambridge, MA 02139, USA
[2]Harvard–MIT Health Sciences and Technology Division, Massachusetts Institute of Technology, Cambridge, MA 02139, USA
[3]Department of Electrical Engineering and Computer Science, Massachusetts Institute of Technology, Cambridge, MA 02139, USA
[4]Department of Chemical Engineering, Massachusetts Institute of Technology, Cambridge, MA 02139, USA
[5]McGovern Institute for Brain Research and Department of Brain and Cognitive Sciences, Massachusetts Institute of Technology, Cambridge, MA 02139, USA
[6]Department of Materials Science and Engineering, Massachusetts Institute of Technology, Cambridge, MA 02139, USA
[7]These authors contributed equally
[8]Lead Contact
*Correspondence: mjcima@mit.edu
https://doi.org/10.1016/j.celrep.2020.107734

SUMMARY

Treatments for neurologic diseases are often limited in efficacy due to poor spatial and temporal control over their delivery. Intracerebral delivery partially overcomes this by directly infusing therapeutics to the brain. Brain structures, however, are nonuniform and irregularly shaped, precluding complete target coverage by a single bolus without significant off-target effects and possible toxicity. Nearly complete coverage is crucial for effective modulation of these structures. We present a framework with computational mapping algorithms for neural drug delivery (COMMAND) to guide multi-bolus targeting of brain structures that maximizes coverage and minimizes off-target leakage. Custom-fabricated chronic neural implants leverage rational fluidic design to achieve multi-bolus delivery in rodents through a single infusion of radioactive tracer (Cu-64). The resulting spatial distributions replicate computed spatial coverage with 5% error *in vivo*, as detected by positron emission tomography. COMMAND potentially enables accurate, efficacious targeting of discrete brain regions.

INTRODUCTION

Targeted delivery of drugs to the brain promises to improve the treatment of intractable neurologic diseases and is an active focus of research (Wolak and Thorne, 2013). Such diseases often arise from dysfunction of specific neural structures, their neuronal and glia populations, and their input-output circuits (Fuccillo, 2016; Godoy et al., 2018; Roozendaal et al., 2009; Wichmann and Dostrovsky, 2011). The efficacy of systemic administration of therapeutics and neurological and neuropsychiatric diseases is limited by control over pharmacokinetics, blood-brain barrier (BBB) penetration, and intracerebral specificity (Wolak and Thorne, 2013). The BBB limits the capacity for many therapeutics to reach the brain without administering doses that risk systemic toxicity (Banks, 2016). Direct intracerebral drug delivery enables increased control over the spatial and temporal delivery profile of therapeutics, especially those that do not cross the BBB and exhibit toxicity systemically or to other off-target brain regions (Tardieu et al., 2017).

Intracerebral delivery entails infusing therapeutics through a single lumen catheter to one point in the brain. This improves targeting over systemic therapy yet has limited capacity to control the spatial distribution of the therapeutic across the target area. Convection-enhanced delivery (CED) relies on high-flow-rate infusion to achieve a uniform distribution of infusate across a large volume. CED has demonstrated potential utility in treating brain malignancies (Souweidane et al., 2018). The high flow rates and large cannula diameters used in CED, however, limit control over the spatial distribution of the infusate and induce trauma along the insertion tract and the cannula outlet. High flow rates, used to generate convective flow, induce damage to tissue near the site of infusion and induce backflow along the insertion tract (Barua et al., 2014, 2015). Large cannula diameters are essential to achieve high flow rates but can lead to inflammation, tissue damage, and scarring around the device, even in acute settings (Spencer et al., 2017).

Many brain structures are irregularly shaped and, therefore, are inadequately served by single point infusions with poor spatial control of infusate distribution. The limitations of single point infusions are hypothesized to underlie the failure of clinical trials for novel neurological therapeutics (Sampson et al., 2010). For example, intracerebroventricular (i.c.v.) and CED delivery of glial-cell-derived neurotrophic factor (GDNF) as a therapy for Parkinson's disease (PD) patients has repeatedly failed to show efficacy in humans, despite promising preclinical studies (Gill et al., 2003; Nutt et al., 2003; Salvatore et al., 2006; Whone

This is an open access article under the CC BY-NC-ND license (http://creativecommons.org/licenses/by-nc-nd/4.0/).

et al., 2019). This failure may have been due to poor GDNF coverage across the target areas, the substantia nigra and caudoputamen.

Targeting specific brain structures in research settings is similarly challenging, as it often depends on stereotaxic techniques and retroactive validation of accurate spatial targeting (Cetin et al., 2006; Correia et al., 2017; Whishaw et al., 1977). Smaller, chronically implanted devices offer superior targeting accuracy compared to acutely inserted needle infusions (Ramadi et al., 2018). Emerging methods allow for more accurate stereotaxic surgery (100 μm to 10 μm resolution) (Blasiak et al., 2010; Li et al., 2013; Ramrath et al., 2008; Rangarajan et al., 2016; Scouten, 2019; Waspe et al., 2010). Methods for determining where to infuse boluses, however, rely on traditional empirical approaches (Barbash et al., 2013; Correia et al., 2017; Uney et al., 1988). Multi-bolus infusions improve control over spatial distribution, which reduces off-target toxicity. However, no standardized method to determine the optimal number, size, and location of boluses for a particular application exists (Cederfjäll et al., 2015; Horellou et al., 1994; Kirik et al., 2000; Wang et al., 2017b).

Here, we describe an approach using multi-bolus delivery for accurate control over spatial coverage of brain infusates. Multiple boluses enable delivery of therapeutic levels of infusate with reduced off-target distribution (Cearley and Wolfe, 2007; Vite et al., 2005). The position and volume of each bolus for targeting a specific structure is optimized using computational mapping algorithms for neural drug delivery (COMMAND) to maximize on-target delivery and minimize off-target leakage. Customizable multi-channel chronic implants are fabricated for targeted delivery of structures *in vivo*. These implants utilize channels with an outer diameter smaller than 100 μm that minimize trauma on insertion (Cotler et al., 2019; Spencer et al., 2017). Our computational approach can be potentially adapted to serve different types of infusates (e.g., small-molecule therapeutics, protein therapeutics, gene therapy, cell therapy, and contrast agents) or for electrical, optical, or acoustic stimulation therapies. Our toolkit could enable spatially targeted modulations to improve our ability to understand and modulate neural activity and, ultimately, more reliable translation of novel therapeutics into the clinic.

RESULTS

Strategic Dosing with Multiple Boluses Enables More Effective Coverage of Irregularly Shaped Brain Structures

Localized drug delivery to focal regions within the brain requires precise targeting with near-complete on-target coverage and limited off-target exposure (Figures 1A and 1B). We chose the striatum as a representative target to explore multi-bolus drug delivery. The striatum is a key node in dopaminergic and cortico-basal ganglia circuitry (Rice et al., 2011; Watabe-Uchida et al., 2012). Striatal dysfunction is indicated in many neurological disorders (DeLong and Wichmann, 2007; Fuccillo, 2016). The striatum is relatively large (60 mm^3 volume in rat) and irregularly shaped (compactness of ~0.7, ratio of striatum volume to volume of sphere with identical surface area). This configuration presents a challenge to achieving complete coverage with a single focal infusion without significant off-target exposure to adjacent tissue, which can cause undesirable toxicity and unwanted effects (Paxinos, 2007).

We explored the utility of multi-bolus delivery in improving targeting accuracy. COMMAND identifies the optimal bolus location and volume for a given brain structure. We first defined two metrics that are jointly minimized to identify the optimal bolus. The first, E_1, indicates the error associated with failing to fill any portion of the target brain structure. The second, E_2, indicates the error associated with delivering drug outside of the target region. Here we assume that the infusate has (1) a minimum effective concentration (MEC) below which it exhibits no therapeutic effect, (2) no toxicity at supratherapeutic concentrations within the target, and (3) dose-dependent toxicity off target. We further assume that the infusate quickly reaches steady-state spatial distribution as previously described for Cu-64 infusions (Ramadi et al., 2018). Alternative assumptions around desired infusate concentrations to balance therapeutic efficacy and off-target toxicity are explored in Figure S1.

COMMAND seeks to identify the optimal location and volume of the desired number of infusions to minimize the combination of the two errors (E_1 and E_2). The second error term (E_2) is weighted by a toxicity penalty, W, which balances the relative importance of minimizing off-target targeting with maximizing target coverage. The overall error, E, is minimized by the algorithm and is defined as the weighted sum of the two error terms as shown in Equation 1:

$$E = E_1 + W * E_2. \quad \text{(Equation 1)}$$

The use of multiple boluses enables greater control over the spatial distribution of the infusate and therefore improves coverage of the target structure. We tested algorithm performance across a range of W (0.1, 0.3, 1, and 2) and selected W = 0.3 as a conservative scenario where both errors could contribute substantially to total error (Figure S2) (Slavc et al., 2018). A 2D simulation demonstrated that a single bolus infusion fails to effectively infiltrate a large part of the striatum (65% coverage) while also delivering some drug outside of the striatum (Figures 1C and 1D). A two bolus infusion more effectively covers the striatum (83% coverage, E_1 decreases by 87%) while also delivering less drug outside of the target region (E_2 decreases by 56%). (Figures 1E and 1F). Both E_1 and E_2 are reduced with two boluses versus a single-bolus infusion (Figure 1G). The addition of an additional bolus improves targeting accuracy and reduces off target error. Many brain structures are irregular in shape (low compactness), indicating that multi-bolus delivery will offer substantial benefit over a single-bolus infusion (Figure 1H).

Computationally Guided Dosing of Multiple Boluses to Various Brain Structures

COMMAND can be expanded to any target structure. We demonstrate the benefit of multiple boluses when targeting

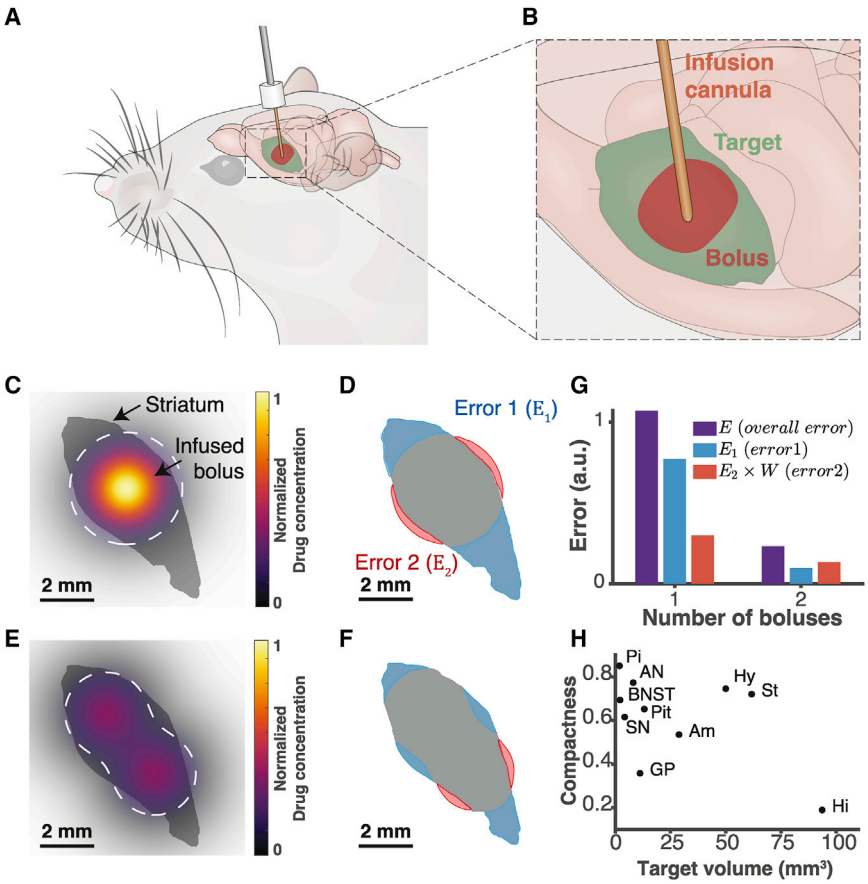

Figure 1. Multi-bolus Delivery Increases Targeting Accuracy

(A) Illustration of single-bolus infusion into rat brain target region (green) via an implanted microdevice.

(B) Expanded view of (A) showing the infusion cannula, bolus-infused, and target region.

(C and D) 2D simulation (C) of single-bolus infusion to striatum and (D) resulting under-dosed target regions (Error 1 (E_1), blue shading) and incorrectly dosed off-target regions (Error 2 (E_2), red shading).

(E and F) 2D simulation (E) of two bolus infusions to striatum and (F) resulting under-dosed target regions (E_1, blue shading) and incorrectly dosed off-target regions (E_2, red shading).

(G) Plot of E_1, E_2, and E for one and two boluses for 2D simulation of striatum targeting. E is a weighted sum of E_1 and E_2. All simulations use $W = 0.3$.

(H) Compactness and volume for various brain structures. Pi, pineal gland; AN, accumbens nucleus; BNST, bed nucleus of stria terminalis; Pit, pituitary gland; SN, substantia nigra; GP, globus pallidus; Hi, hippocampus; Hy, hypothalamus; St, striatum; Am, amygdala.

3D brain structures by computing the optimal dose for the striatum, amygdala, substantia nigra, and hippocampus when using one to four boluses (Figure 2A). We used the entire contiguous hippocampus due to its very low compactness. We allowed the position, volume, and number of boluses to vary while holding infusate concentration constant. The use of multiple boluses allowed for more accurate targeting of irregularly shaped structures. The overall error decreased with more boluses (Figure 2B). Generally, the errors associated with targeting the structure and off-target exposure also decreased with an increased number of boluses. Within the striatum, for example, the addition of a second and third bolus increased the coverage of the target region by ~30% and 50% while minimally affecting off-target dosing.

For compact structures (i.e., striatum, amygdala, and substantia nigra), more boluses allowed a similar volume of drug to be distributed more effectively (Figure 2C). For the less compact structure (i.e., hippocampus), additional boluses improved coverage by increasing total volume infused rather than redistributing infusate. The marginal utility of additional boluses depended on the shape of the structure (Figure 2D). For the hippocampus, additional boluses consistently improved targeting across the tested range. The substantia nigra, in contrast, showed little improvement after the second bolus. In some cases, the error associated with off-target toxicity increased with additional boluses. The highly irregular structure of the hippocampus resulted in each additional bolus improving coverage while minimally contributing to off-target exposure. Despite this, the overall error consistently decreased with additional boluses. Increasing the toxicity penalty shifts the balance from allowing off-target exposure to instead avoiding it at the expense of complete target coverage. The error associated with off-target exposure decreased with increasing toxicity penalty (Figure S2). The coverage volume consistently decreased with increased toxicity penalty.

Localization and Detection of Multiple Drug Boluses in the Brain via PET

Microliter-scale boluses delivered to the brain require a highly sensitive method for noninvasive imaging. Prior work has utilized positron emission tomography (PET) to examine the spatiotemporal dynamics of single boluses after intracerebral infusion (Ramadi et al., 2018). A similar approach was used to identify and localize multiple adjacent boluses. We characterized the ability of PET to detect distinct boluses with varying inter-bolus distances. Pairs of Cu-64 solution boluses were simultaneously infused into brain phantoms via implanted microcapillaries (Figures 3A and S3). The distances between the pairs of boluses were varied from 1 to 4 mm, and the inter-bolus distance estimated from PET images was compared to the true inter-bolus distance. PET images identified distinct adjacent boluses with inter-bolus distance as low as 1 mm (Figures 3A–3E).

We conducted similar experiments *in vivo* with chronically implanted fused silica capillaries, which showed that PET can

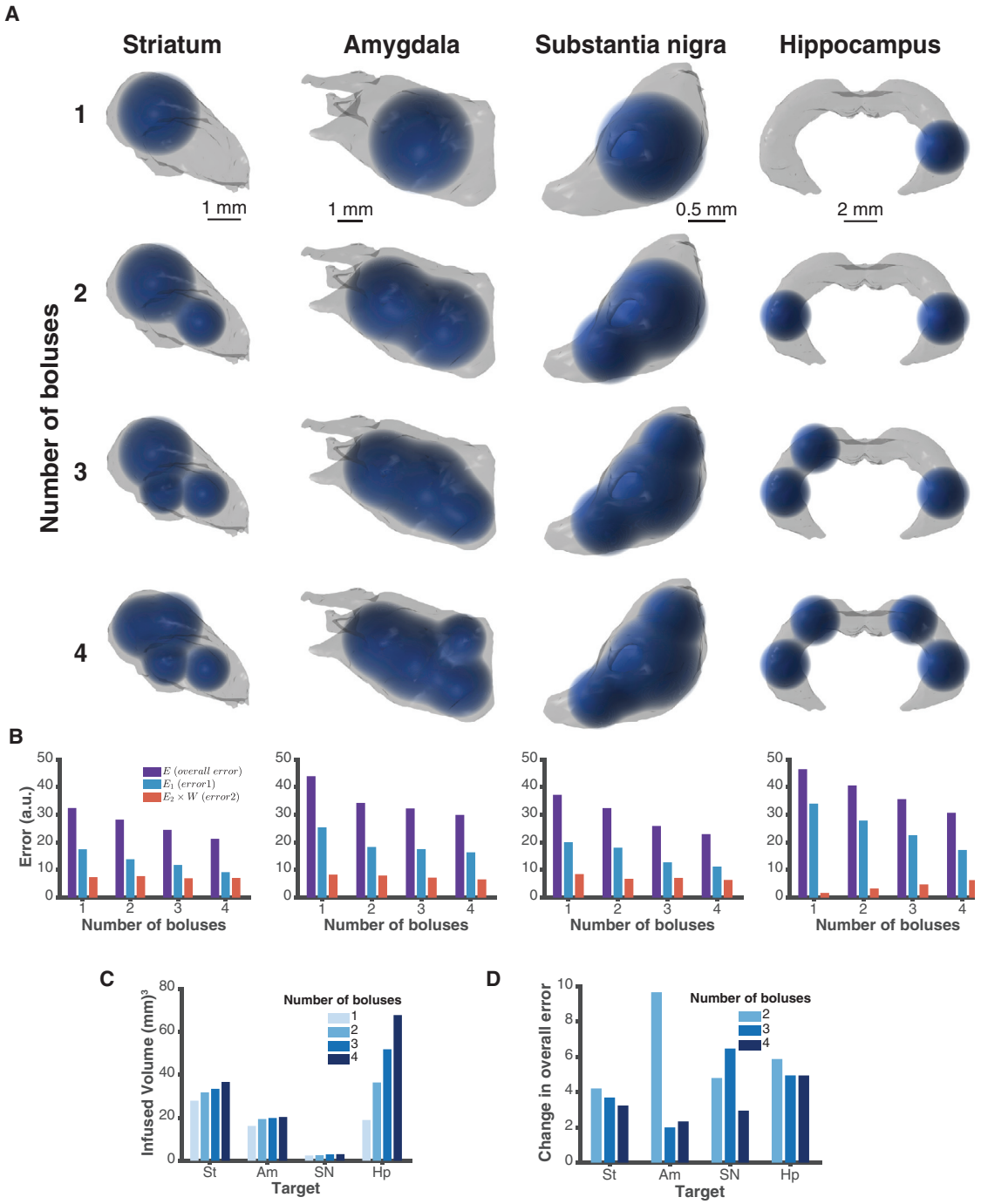

Figure 2. 3D Computational Simulations of Multi-bolus Targeting of Brain Structures Using COMMAND

(A) 3D renderings of simulated multi-bolus delivery to various brain structures (striatum, amygdala, substantia nigra, and hippocampus) with one to four boluses. Boluses show volumes dosed at or above 10% of peak infused drug concentration.

(B) E_1, E_2, and E versus number of boluses for each target structure. E is a weighted sum of E_1 and E_2. All simulations use $W = 0.3$.

(C) Volume infused in simulations for targeting structures with one to four boluses.

(D) Incremental change in overall error with each additional bolus for various structures.

See also Figure S2.

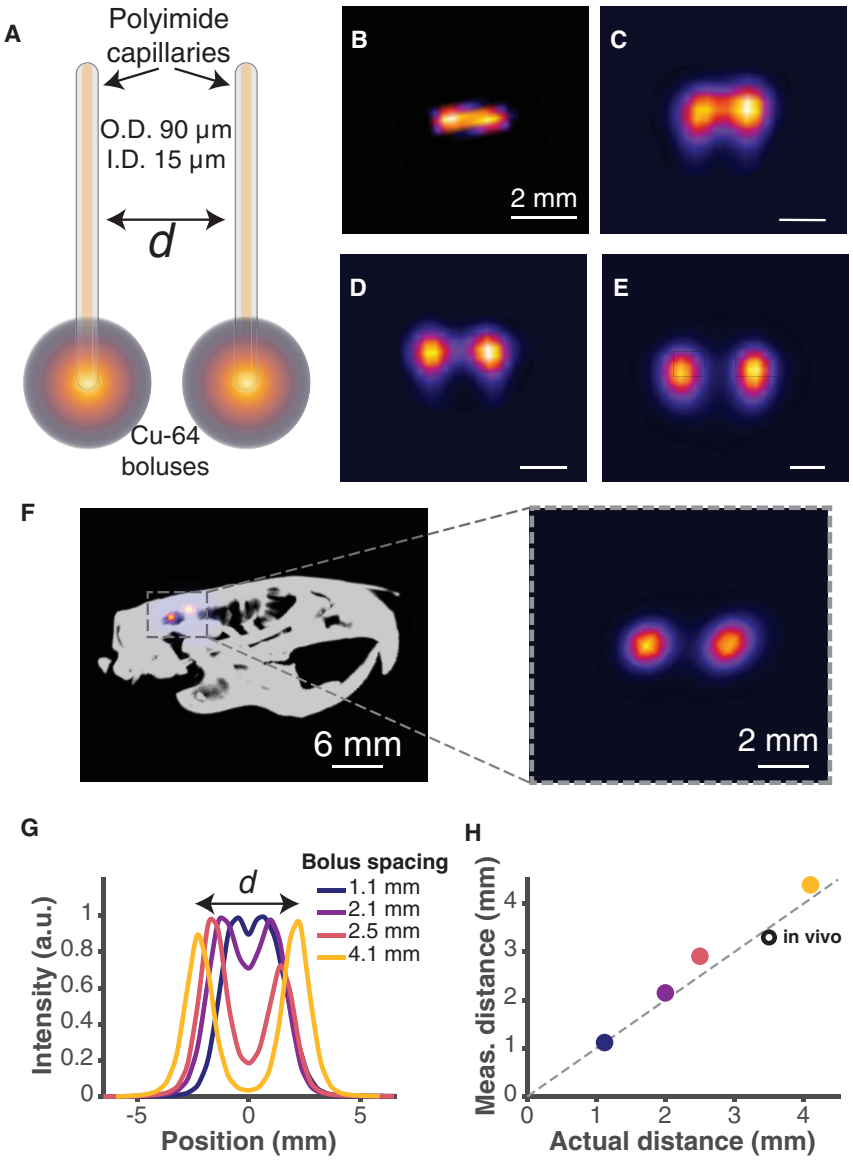

Figure 3. PET Imaging Identifies Distinct Microliter Boluses 1–4 mm Apart

(A) Illustration of two adjacent capillaries at variable distance, *d*, apart. Identical boluses (1.67 µL) were infused through each simultaneously.

(B–E) PET images showing transverse sections of adjacent boluses at separation distances of (B) 1.1 mm, (C) 2 mm, (D) 2.5 mm, and (E) 4.1 mm.

(F) PET/computed tomography (CT) image showing rat skull overlaid with two boluses injected into brain simultaneously at a particular separation distance. Inset shows PET image of two identical boluses.

(G) Line profiles extracted from PET images indicating variable peak-to-peak distance corresponding to bolus separation, *d*.

(H) Plot of measured distance computed from PET images versus actual distance between capillary outlets. The identity line (dashed gray) shows theoretical ideal agreement between measured and actual distance.

I.D., inner diameter, O.D., outer diameter.

discriminate and accurately localize the relative location of two adjacent Cu-64 boluses (Figure 3F). Line profiles across each pair of boluses derived from PET images identified and estimated the inter-bolus distance to within a mean error of 8% accuracy (Figures 3G and 3H). Microcapillaries were implanted up to 2 months and used repeatedly, with no clogging detected.

We also characterized gliosis surrounding the chronic implant and show limited astrocyte and microglial accumulation surrounding the implant (Figure S3). These data validate the use of micro-implants for chronic, repeated infusions and PET to visualize and characterize multi-bolus delivery.

Leveraging Fluidic Resistance for Simultaneous, Variable Multi-bolus Volumes through a Single Infusion

We leveraged the results from COMMAND to inform the design of a device that enables simultaneous delivery of multiple adjacent boluses *in vivo*. Sequential delivery of each bolus could result in time delays potentially compromising the ability of rapidly metabolized or transported infusates to modulate the target structure (Ramadi et al., 2018). We sought to overcome this limitation by designing multi-channel devices capable of reproducing both the locations and volumes of each bolus described by the computational algorithm (Figure S4). Each device consisted of multiple distinct cannulas with lumen outlets arranged to match the intended spatial distribution of boluses (Figure 4A). Each cannula was connected via a variable length of tubing to a single infusion line. Channels with inner diameters of 15 µm were the dominant source of fluid resistance in the system (Figure 4B). Simultaneous delivery of multiple boluses of different volumes was achieved by controlling the relative fluidic resistance across each channel. The length of each channel was specified to control its fluidic resistance. The relative volume of infusate delivered at each outlet was proportional to the ratio of resistances between channels (Figure 4B).

We validated this approach by implanting a two-channel device in a phantom and infusing 1.67 µL of Cu-64. Infused volumes measured via quantitative PET matched theoretical infusion volumes based on device design (<2% error) (Figures 4C–4E). Leveraging hydraulic resistance when designing neural drug delivery probes enables independent control over the position and volume of each bolus while also allowing for delivery via a single infusion.

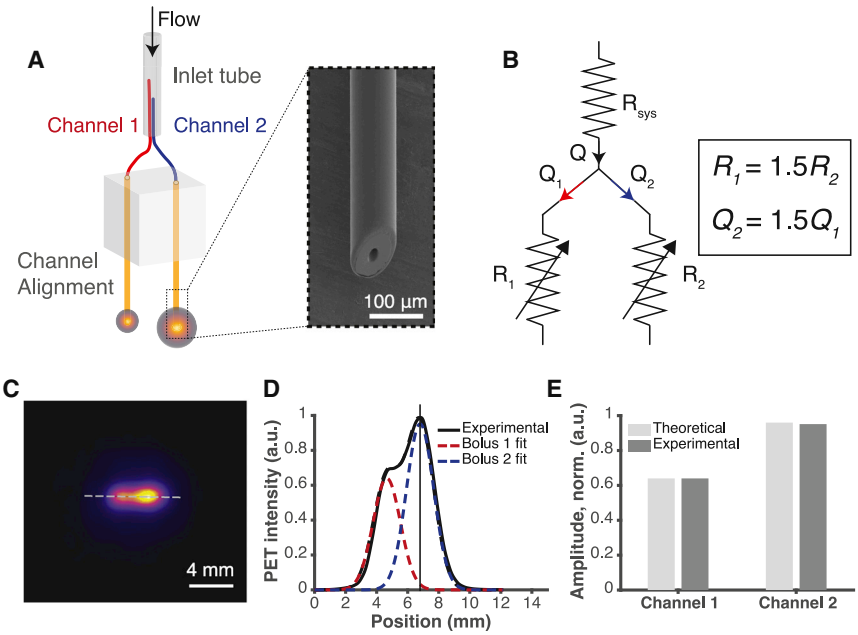

Figure 4. Rational Fluidic Design Enables Simultaneous Multi-bolus Infusions

(A) Illustration of a two-channel device with a single fluidic input. Inset: scanning electron micrograph of the tip of the fused silica/polyimide probe.

(B) Analogous circuit diagram showing fluidic resistances of each channel, R_1 and R_2, with corresponding flow rates Q_1 and Q_2.

(C) Maximum intensity projection PET image of Cu-64 infused through the implanted device shown in (A) into agarose.

(D) Line profile derived from a PET image (black) versus position across the major axis with constituent boluses (red, blue) estimated via best fit of the two-bolus model.

(E) Intensity of predicted (from device design) and measured (from PET) boluses.

See also Figure S3.

Computationally Guided *In Vivo* Targeting of Rodent Striatum through Multi-channel Devices

Prior state-of-the-art efforts to target the striatum via intracerebral infusion use a highly variable number of boluses and infusion volumes (Figures 5A, 5B, and S5). The high variability persists even when considering studies utilizing similar infusates. This suggests a lack of consensus in the optimal infusion strategy for striatal targeting.

We implemented a similar technique to target the striatum of rats via a single bolus infusion of Cu-64 solution (1.67 µL, 0.167 µL/min) via a chronically implanted (>1 week) capillary. We examined the spatial extent of this bolus with respect to the target brain structure via PET (Figures 5C and 5D). The bolus did not cover a substantial portion of the striatum despite exceeding the boundaries of the target along the medio-lateral axis.

We next designed and implanted devices for targeting the striatum with two and three boluses of Cu-64 (Figure 5E). We implanted these in rats and used the established relationship between infused Cu-64 volume and tissue coverage volume to determine the volume to be infused for a desired radius of effect (Dagdeviren et al., 2018). We infused Cu-64 (2.6 and 3.1 µL for two and three boluses, respectively) through chronically implanted multi-channel devices and characterized the resultant infusion profile via PET. PET images and 3D reconstructions overlaid with the striatum demonstrate that the multi-bolus infusion within the target region improves target coverage (Figures 5F–5I). We validated the accuracy of the multi-bolus infusion by comparing the volume of tissue exposed to infusate against the desired coverage volume specified by COMMAND (Figure 5J). The experimentally observed volume of drug above MEC did not significantly differ from the computational simulation in the case of two boluses (n = 7, p = 0.400, two-sided t test) or three boluses (n = 8, p = 0.388, two-sided t test). The experimentally measured coverage volume matches the simulated volume (<5% error) and increases significantly from two to three boluses (n = 15, p = 0.012, one-sided t test).

DISCUSSION

COMMAND is a computational framework for targeting irregularly shaped structures that cannot be completely dosed from single infusion boluses without significant off-target exposure. Neuroscience studies involving the use of intracerebral infusions use empirical, geometric methods to determine the size and location of each infusion. This approach, however, is not appropriate for many brains targets given the diversity of shapes and sizes of structures, and results in significant variability across studies targeting the same structure (Figure S5) (Allen Institute, 2016). The utility of COMMAND is that the targeting can be automatically calculated, giving accuracy in focusing on targets of any shape. We demonstrate this advantage by guiding delivery to the striatum in rats using devices with multiple infusion lumens. Our approach leveraged varying fluidic resistance of individual channels to achieve multi-bolus delivery through a single infusion. These devices achieved ~5% accuracy experimentally when compared to the theoretical infusion volume.

A practical consideration in determining the optimal number of infusion points is that a greater number implies more insertion trauma. The relative utility of increasing the number of infusion boluses follows a trend of diminishing marginal return (Figures 2B and 2D). Optimal therapeutic outcomes involve a tradeoff between invasiveness (number of infusions sites) and therapeutic benefit (accurate target coverage). Multi-contact electrodes, multi-lumen capillaries, or curved insertion trajectories could be utilized for specific cases to target various points through a single insertion point, reducing invasiveness and trauma (Cotler et al., 2019). A significant source of targeting error also arises

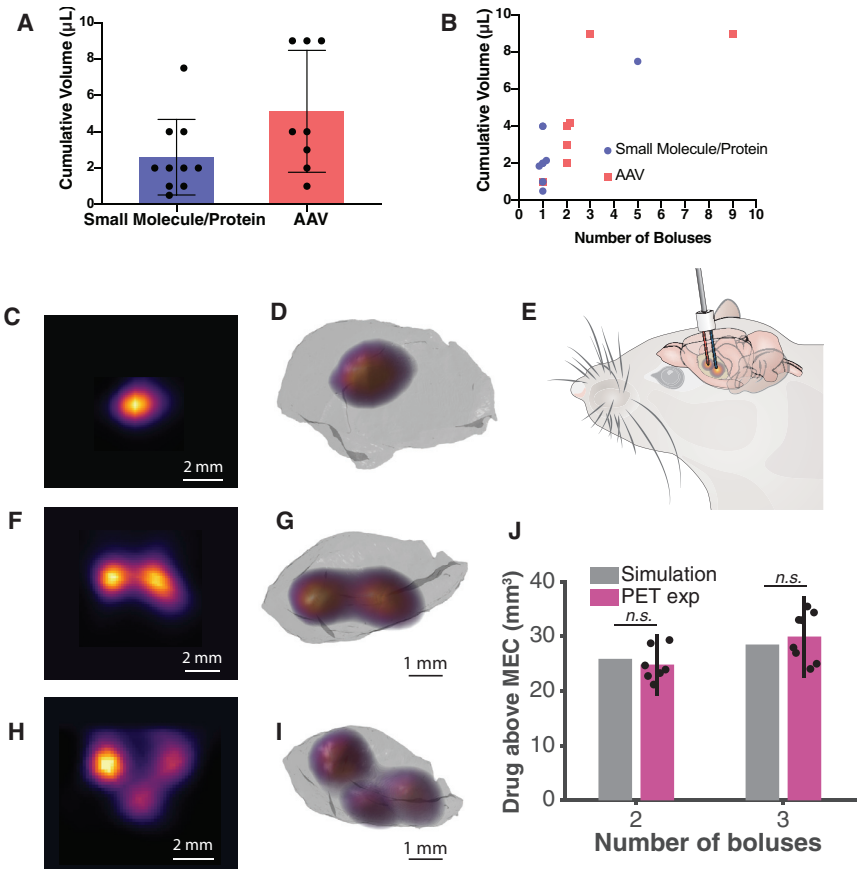

Figure 5. Computationally Guided Multi-bolus Targeting of Striatum *In Vivo*

(A and B) Prior efforts for intrastriatal targeting via fluidic injection.

(C) PET maximum intensity projection of a single bolus infused into rat brain.

(D) PET-derived 3D concentration profile of a single bolus overlaid on striatum.

(E) Illustration of multi-bolus targeting of brain structure through a chronically implanted device.

(F) PET maximum intensity projection of two-bolus delivery targeting the striatum.

(G) PET-derived 3D concentration profile of two-bolus infusion overlaid on striatum.

(H) PET maximum intensity projection of three-bolus delivery targeting the striatum.

(I) PET-derived 3D concentration profile of three-bolus infusion overlaid on striatum.

(J) Simulated and PET-derived experimental coverage volume for two-bolus (n = 7, p = 0.400) and three-bolus (n = 8, p = 0.388) experiments. Error bars indicate 95% confidence intervals. n.s., not significant, assessed via two-sided t test. See also Figures S4–S6.

from backflow when using acutely inserted catheters (Sampson et al., 2010). Here, we used chronically implanted devices to ensure focal delivery with minimal backflow. The capillaries were sufficiently small to minimize gliosis as chronic implants (Spencer et al., 2017). The small diameter also allowed us to vary the fluidic resistance of each channel to guide fluid flow from a single infusion (Figure 4). If larger probes are used, other sources of fluidic resistance may dominate, preventing a similar strategy for fluid control across multiple boluses. Our work implemented capillaries of identical diameter and varying lengths as a means to control relative distribution of fluid flow. One could also change the inner diameter of an individual capillary to enhance further any desired difference in flow. This approach can be used in all cases where the fluidic resistance of the capillaries is at least 10 times larger than any other circuit resistance. Intracranial pressures, for example, are ~7–15 mmHg, with fluctuations on the order of 1 mmHg (Albeck et al., 1991). By comparison, pressure head across our capillaries at the flow rates and viscosities used here range from 170 to 1700 mmHg. These techniques assume laminar flow (Reynolds number <2,000) and incompressible, Newtonian fluid flow. At high drug concentrations, it may be possible see deviation from Newtonian behavior. In this case, one could accommodate this by using lower flow rates or capturing this behavior within the computational model. It is also important that all multi-channel implants must be designed such that each catheter outlet is implanted relative to standard stereotactic references of bregma or lambda. Referencing catheter positions to each other should be avoided to prevent tolerance stacking and propagation of errors.

This COMMAND framework could further be refined by incorporating heterogeneity of the regions surrounding the target structure. Certain structures adjacent to the target, such as a ventricle or white matter tract, will result in anisotropic diffusion (Lam et al., 2011). Another example where surrounding heterogeneity could be important is if off-target dosing of an adjacent structure would have severe adverse effects and therefore would have to be avoided. One could modify the objective function of the computational approach to penalize such exposure more severely than off-target exposure to other regions. This approach could enable superior targeting of certain structures with well-defined functional boundaries such as the cingulate sulcus (Amemori and Graybiel, 2012). Similarly, the accuracy of COMMAND is dependent on appropriate choice of brain atlas. Different species and breeds can have significantly differing brain anatomies (Calabrese et al., 2013; Paxinos, 2007). In cases where even higher precision is desired, magnetic resonance imaging (MRI) brain mapping could yield a subject specific atlas to account for individual anatomical variability.

COMMAND is potentially translatable for optimization of other drugs and infusates, including cell-based therapies, as well as other neuromodulation modalities including electrical, optical, and acoustic simulation (Haywood et al., 2019; Iliff et al., 2012; Owen et al., 2019; Pollo et al., 2014; Szablowski et al., 2018). COMMAND is most effective with a reliable calibration curve established on a drug-by-drug basis based on empirical behavior examined in the target brain region. We conducted similar simulations modeling intracranial delivery of light

for potential use in optogenetics (Figure S6). We simulated a single optical fiber for each brain region using a flat-faced optical fiber and sought to maximize on-target coverage by varying the position and fiber angle along the coronal and sagittal planes. The optical illumination profile was highly anisotropic due to the strongly dominant forward scattering observed in neural tissue which can be summarized with the anisotropy index (Yona et al., 2016). COMMAND may also be applied to other modalities, such as electrical or thermal deep brain simulation. We can build a simulation environment to parameterize and predict spatial distributions of each modality using equations governing heat flow and electrical propagation in tissue. We would ideally have *in vivo* biological validation of each simulation environment used in the COMMAND framework; however, it may be challenging to acquire high precision *in vivo* data across a variety of modalities and parameters in neural tissue.

The adaptability of our approach is particularly important when transitioning from rodents to larger species (e.g., non-human primates, humans). Few clinical trials have investigated the therapeutic window of specific drugs in the brain due to difficulties in controlling distribution and delivery, in marked contrast to the extensive pharmacokinetic studies performed for systemically administered agents. Our toolkit could be beneficial in testing and establishing such windows. A similar technique could be applied to the delivery of any substance or energy where the spatial distribution within tissue can be characterized, including electrical stimuli, radiation, light, or mechanical energy (e.g., ultrasound). The modality (e.g., substance or energy) and the desired effect (e.g., modulation, tissue ablation, etc.) would affect the choice of appropriate toxicity penalty employed in the simulation. Ablation of an epileptogenic focus or silencing of the substantia nigra, for example, necessitates complete coverage of the target at the expense of some surrounding healthy tissue (i.e., a relatively low value of toxicity penalty) (Curry et al., 2012; Ramadi et al., 2018).

In summary, we have developed a computational approach that enables identification of the optimal multi-bolus dose to fill a target brain structure. We used this algorithm to inform device design and demonstrate accurate *in vivo* targeting of the striatum with two and three boluses. This approach generalizes across target structures and species for which detailed brain atlases and precise stereotaxic navigation exist. COMMAND provides a versatile framework for both researchers and, ultimately, clinicians to improve spatial targeting of irregularly shaped brain structures via intracerebral targeting.

STAR★METHODS

Detailed methods are provided in the online version of this paper and include the following:

- KEY RESOURCES TABLE
- RESOURCE AVAILABILITY
  - Lead Contact
  - Materials Availability
  - Data and Code Availability
- EXPERIMENTAL MODELS AND SUBJECT DETAILS
- METHOD DETAILS
  - COMMAND: Algorithm and computational approach
  - Optical simulation
  - Characterizing brain structure irregularity
  - Device Fabrication
  - Device implantation in rats
  - PET infusions, imaging, and reconstruction
  - Chronic *In Vivo* Biocompatibility Assessment
  - Histology Protocol of Chronic *In Vivo* Biocompatibility
- QUANTIFICATION AND STATISTICAL ANALYSIS

SUPPLEMENTAL INFORMATION

Supplemental Information can be found online at https://doi.org/10.1016/j.celrep.2020.107734.

ACKNOWLEDGMENTS

We thank Howard Mak of the Animal Imaging Core Facility at the Koch Institute for Integrative Cancer Research for his assistance with PET imaging. This work is supported by the National Institutes of Health, National Institute of Biomedical Imaging and Bioengineering (R01 EB016101 to R.L., A.M.G., and M.J. Cima), and in part by the National Cancer Institute (P30-CA14051 to the Koch Institute Core). A.B. was supported by graduate fellowships from the Fannie & John Hertz Foundation and National Science Foundation.

AUTHOR CONTRIBUTIONS

K.B.R., A.B., R.L., A.M.G., and M.J. Cima designed research; K.B.R., A.B., C.J.F., E.B.R., and M.J. Cotler, performed research; K.B.R., A.B., C.J.F., E.B.R., and M.J. Cotler analyzed data; K.B.R., A.B., C.J.F., E.B.R., R.L., A.M.G, and M.J. Cima wrote the paper.

DECLARATION OF INTERESTS

The authors declare no competing interests.

Received: November 12, 2019
Revised: February 24, 2020
Accepted: May 13, 2020
Published: June 9, 2020

REFERENCES

Albeck, M.J., Børgesen, S.E., Gjerris, F., Schmidt, J.F., and Sørensen, P.S. (1991). Intracranial pressure and cerebrospinal fluid outflow conductance in healthy subjects *74*, 597.

Allen Institute (2016). Injection Sites and Stereotaxic Coordinates for Anterograde Projectome (Brain-Wide) (Allen Institute for Brain Science).

Amemori, K., and Graybiel, A.M. (2012). Localized microstimulation of primate pregenual cingulate cortex induces negative decision-making. Nat. Neurosci. *15*, 776–785.

Aoi, M., Date, I., Tomita, S., and Ohmoto, T. (2000). The effect of intrastriatal single injection of GDNF on the nigrostriatal dopaminergic system in hemiparkinsonian rats: behavioral and histological studies using two different dosages. Neurosci. Res. *36*, 319–325.

Banks, W.A. (2016). From blood-brain barrier to blood-brain interface: new opportunities for CNS drug delivery. Nat. Rev. Drug Discov. *15*, 275–292.

Barbash, S., Hanin, G., and Soreq, H. (2013). Stereotactic injection of microRNA-expressing lentiviruses to the mouse hippocampus ca1 region and assessment of the behavioral outcome. J. Vis. Exp. *76*, e50170.

Barua, N.U., Gill, S.S., and Love, S. (2014). Convection-enhanced drug delivery to the brain: therapeutic potential and neuropathological considerations. Brain Pathol. *24*, 117–127.

Barua, N.U., Bienemann, A.S., Woolley, M., Wyatt, M.J., Johnson, D., Lewis, O., Irving, C., Pritchard, G., and Gill, S. (2015). Convection-enhanced delivery of MANF–volume of distribution analysis in porcine putamen and substantia nigra. J. Neurol. Sci. *357*, 264–269.

Bilang-Bleuel, A., Revah, F., Colin, P., Locquet, I., Robert, J.-J., Mallet, J., and Horellou, P. (1997). Intrastriatal injection of an adenoviral vector expressing glial-cell-line-derived neurotrophic factor prevents dopaminergic neuron degeneration and behavioral impairment in a rat model of Parkinson disease. Proc. Natl. Acad. Sci. USA *94*, 8818–8823.

Blasiak, T., Czubak, W., Ignaciak, A., and Lewandowski, M.H. (2010). A new approach to detection of the bregma point on the rat skull. J. Neurosci. Methods *185*, 199–203.

Calabrese, E., Badea, A., Watson, C., and Johnson, G.A. (2013). A quantitative magnetic resonance histology atlas of postnatal rat brain development with regional estimates of growth and variability. Neuroimage *71*, 196–206.

Cearley, C.N., and Wolfe, J.H. (2007). A single injection of an adeno-associated virus vector into nuclei with divergent connections results in widespread vector distribution in the brain and global correction of a neurogenetic disease. J. Neurosci. *27*, 9928–9940.

Cederfjäll, E., Broom, L., and Kirik, D. (2015). Controlled striatal DOPA production from a gene delivery system in a rodent model of Parkinson's disease. Mol. Ther. *23*, 896–906.

Cetin, A., Komai, S., Eliava, M., Seeburg, P.H., and Osten, P. (2006). Stereotaxic gene delivery in the rodent brain. Nat. Protoc. *1*, 3166–3173.

Correia, P.A., Matias, S., and Mainen, Z.F. (2017). Stereotaxic adeno-associated virus injection and cannula implantation in the dorsal raphe nucleus of mice. Bio. Protoc. *7*, e2549.

Cotler, M.J., Rousseau, E.B., Ramadi, K.B., Fang, J., Graybiel, A.M., Langer, R., and Cima, M.J. (2019). Steerable microinvasive probes for localized drug delivery to deep tissue. Small *15*, e1901459.

Curry, D.J., Gowda, A., McNichols, R.J., and Wilfong, A.A. (2012). MR-guided stereotactic laser ablation of epileptogenic foci in children. Epilepsy Behav. *24*, 408–414.

Dagdeviren, C., Ramadi, K.B., Joe, P., Spencer, K., Schwerdt, H.N., Shimazu, H., Delcasso, S., Amemori, K.I., Nunez-Lopez, C., Graybiel, A.M., et al. (2018). Miniaturized neural system for chronic, local intracerebral drug delivery. Sci. Transl. Med. *10*, eaan2742.

DeLong, M.R., and Wichmann, T. (2007). Circuits and circuit disorders of the basal ganglia. Arch. Neurol. *64*, 20–24.

Fuccillo, M.V. (2016). Striatal circuits as a common node for autism pathophysiology. Front. Neurosci. *10*, 27.

Gill, S.S., Patel, N.K., Hotton, G.R., O'Sullivan, K., McCarter, R., Bunnage, M., Brooks, D.J., Svendsen, C.N., and Heywood, P. (2003). Direct brain infusion of glial cell line-derived neurotrophic factor in Parkinson disease. Nat. Med. *9*, 589–595.

Godoy, L.D., Rossignoli, M.T., Delfino-Pereira, P., Garcia-Cairasco, N., and de Lima Umeoka, E.H. (2018). A comprehensive overview on stress neurobiology: basic concepts and clinical implications. Front. Behav. Neurosci. *12*, 127.

Hattori, A., Luo, Y., Umegaki, H., Munoz, J., and Roth, G.S. (1998). Intrastriatal injection of dopamine results in DNA damage and apoptosis in rats. Neuroreport *9*, 2569–2572.

Haywood, T., Beinat, C., Gowrishankar, G., Patel, C.B., Alam, I.S., Murty, S., and Gambhir, S.S. (2019). Positron emission tomography reporter gene strategy for use in the central nervous system. Proc. Natl. Acad. Sci. USA *116*, 11402–11407.

Horellou, P., Vigne, E., Castel, M.N., Barnéoud, P., Colin, P., Perricaudet, M., Delaère, P., and Mallet, J. (1994). Direct intracerebral gene transfer of an adenoviral vector expressing tyrosine hydroxylase in a rat model of Parkinson's disease. Neuroreport *6*, 49–53.

Iliff, J.J., Wang, M., Liao, Y., Plogg, B.A., Peng, W., Gundersen, G.A., Benveniste, H., Vates, G.E., Deane, R., Goldman, S.A., et al. (2012). A paravascular pathway facilitates CSF flow through the brain parenchyma and the clearance of interstitial solutes, including amyloid β. Sci. Transl. Med. *4*, 147ra111.

Kilbourn, M.R., Charalambous, A., Frey, K.A., Sherman, P., Higgins, D.S., Jr., and Greenamyre, J.T. (1997). Intrastriatal neurotoxin injections reduce in vitro and in vivo binding of radiolabeled rotenoids to mitochondrial complex I. J. Cereb. Blood Flow Metab. *17*, 265–272.

Kirik, D., Rosenblad, C., Björklund, A., and Mandel, R.J. (2000). Long-term rAAV-mediated gene transfer of GDNF in the rat Parkinson's model: intrastriatal but not intranigral transduction promotes functional regeneration in the lesioned nigrostriatal system. J. Neurosci. *20*, 4686–4700.

Lam, M.F., Thomas, M.G., and Lind, C.R. (2011). Neurosurgical convection-enhanced delivery of treatments for Parkinson's disease. J. Clin. Neurosci. *18*, 1163–1167.

Li, X., Aggarwal, M., Hsu, J., Jiang, H., and Mori, S. (2013). AtlasGuide: software for stereotaxic guidance using 3D CT/MRI hybrid atlases of developing mouse brains. J. Neurosci. Methods *220*, 75–84.

Luo, Y., Hattori, A., Munoz, J., Qin, Z.H., and Roth, G.S. (1999). Intrastriatal dopamine injection induces apoptosis through oxidation-involved activation of transcription factors AP-1 and NF-kappaB in rats. Mol. Pharmacol. *56*, 254–264.

Mandel, R.J., Rendahl, K.G., Spratt, S.K., Snyder, R.O., Cohen, L.K., and Leff, S.E. (1998). Characterization of intrastriatal recombinant adeno-associated virus-mediated gene transfer of human tyrosine hydroxylase and human GTP-cyclohydrolase I in a rat model of Parkinson's disease. J. Neurosci. *18*, 4271–4284.

Nutt, J.G., Burchiel, K.J., Comella, C.L., Jankovic, J., Lang, A.E., Laws, E.R., Jr., Lozano, A.M., Penn, R.D., Simpson, R.K., Jr., Stacy, M., and Wooten, G.F.; ICV GDNF Study Group. Implanted intracerebroventricular. Glial cell line-derived neurotrophic factor (2003). Randomized, double-blind trial of glial cell line-derived neurotrophic factor (GDNF) in PD. Neurology *60*, 69–73.

Owen, S.F., Liu, M.H., and Kreitzer, A.C. (2019). Thermal constraints on in vivo optogenetic manipulations. Nat. Neurosci. *22*, 1061–1065.

Paxinos, G.W.C. (2007). The Rat Brain in Stereotaxic Coordinates, Sixth Edition (Academic Press).

Pollo, C., Kaelin-Lang, A., Oertel, M.F., Stieglitz, L., Taub, E., Fuhr, P., Lozano, A.M., Raabe, A., and Schüpbach, M. (2014). Directional deep brain stimulation: an intraoperative double-blind pilot study. Brain *137*, 2015–2026.

Ramadi, K.B., Dagdeviren, C., Spencer, K.C., Joe, P., Cotler, M., Rousseau, E., Nunez-Lopez, C., Graybiel, A.M., Langer, R., and Cima, M.J. (2018). Focal, remote-controlled, chronic chemical modulation of brain microstructures. Proc. Natl. Acad. Sci. USA *115*, 7254–7259.

Ramrath, L., Hofmann, U.G., and Schweikard, A. (2008). A robotic assistant for stereotactic neurosurgery on small animals. Int. J. Med. Robot. *4*, 295–303.

Rangarajan, J.R., Vande Velde, G., van Gent, F., De Vloo, P., Dresselaers, T., Depypere, M., van Kuyck, K., Nuttin, B., Himmelreich, U., and Maes, F. (2016). Image-based in vivo assessment of targeting accuracy of stereotactic brain surgery in experimental rodent models. Sci. Rep. *6*, 38058.

Rice, M.E., Patel, J.C., and Cragg, S.J. (2011). Dopamine release in the basal ganglia. Neuroscience *198*, 112–137.

Rodrigues, R.W.P., Gomide, V., and Chadi, G. (2003). Striatal injection of 6-hydroxydopamine induces retrograde degeneration and glial activation in the nigrostriatal pathway. Acta Cir. Bras. *18*, 272–282.

Roozendaal, B., McEwen, B.S., and Chattarji, S. (2009). Stress, memory and the amygdala. Nat. Rev. Neurosci. *10*, 423–433.

Sacaan, A.I., Monn, J.A., and Schoepp, D.D. (1991). Intrastriatal injection of a selective metabotropic excitatory amino acid receptor agonist induces contralateral turning in the rat. J. Pharmacol. Exp. Ther. *259*, 1366–1370.

Salvatore, M.F., Ai, Y., Fischer, B., Zhang, A.M., Grondin, R.C., Zhang, Z., Gerhardt, G.A., and Gash, D.M. (2006). Point source concentration of GDNF may explain failure of phase II clinical trial. Exp. Neurol. *202*, 497–505.

Sampson, J.H., Archer, G., Pedain, C., Wembacher-Schröder, E., Westphal, M., Kunwar, S., Vogelbaum, M.A., Coan, A., Herndon, J.E., Raghavan, R., et al.; PRECISE Trial Investigators (2010). Poor drug distribution as a possible explanation for the results of the PRECISE trial. J. Neurosurg. *113*, 301–309.

Shewchuk, J.R. (2002). Delaunay refinement algorithms for triangular mesh generation. Comput. Geom. *22*, 21–74.

Shults, C.W., Kimber, T., and Martin, D. (1996). Intrastriatal injection of GDNF attenuates the effects of 6-hydroxydopamine. Neuroreport *7*, 627–631.

Slavc, I., Cohen-Pfeffer, J.L., Gururangan, S., Krauser, J., Lim, D.A., Maldaun, M., Schwering, C., Shaywitz, A.J., and Westphal, M. (2018). Best practices for the use of intracerebroventricular drug delivery devices. Mol. Genet. Metab. *124*, 184–188.

Souweidane, M.M., Kramer, K., Pandit-Taskar, N., Zhou, Z., Haque, S., Zanzonico, P., Carrasquillo, J.A., Lyashchenko, S.K., Thakur, S.B., Donzelli, M., et al. (2018). Convection-enhanced delivery for diffuse intrinsic pontine glioma: a single-centre, dose-escalation, phase 1 trial. Lancet Oncol. *19*, 1040–1050.

Spencer, K.C., Sy, J.C., Ramadi, K.B., Graybiel, A.M., Langer, R., and Cima, M.J. (2017). Characterization of mechanically matched hydrogel coatings to improve the biocompatibility of neural implants. Sci. Rep. *7*, 1952.

Szablowski, J.O., Lee-Gosselin, A., Lue, B., Malounda, D., and Shapiro, M.G. (2018). Acoustically targeted chemogenetics for the non-invasive control of neural circuits. Nat. Biomed. Eng. *2*, 475–484.

Tardieu, M., Zérah, M., Gougeon, M.L., Ausseil, J., de Bournonville, S., Husson, B., Zafeiriou, D., Parenti, G., Bourget, P., Poirier, B., et al. (2017). Intracerebral gene therapy in children with mucopolysaccharidosis type IIIB syndrome: an uncontrolled phase 1/2 clinical trial. Lancet Neurol. *16*, 712–720.

Uney, J.B., Leigh, P.N., Marsden, C.D., Lees, A., and Anderton, B.H. (1988). Stereotaxic injection of kainic acid into the striatum of rats induces synthesis of mRNA for heat shock protein 70. FEBS Lett. *235*, 215–218.

Vite, C.H., McGowan, J.C., Niogi, S.N., Passini, M.A., Drobatz, K.J., Haskins, M.E., and Wolfe, J.H. (2005). Effective gene therapy for an inherited CNS disease in a large animal model. Ann. Neurol. *57*, 355–364.

Wang, L., Wang, Z., Xu, X., Zhu, R., Bi, J., Liu, W., Feng, X., Wu, H., Zhang, H., Wu, J., et al. (2017a). Recombinant AAV8-mediated intrastriatal gene delivery of CDNF protects rats against methamphetamine neurotoxicity. Int. J. Med. Sci. *14*, 340–347.

Wang, L., Wang, Z., Zhu, R., Bi, J., Feng, X., Liu, W., Wu, J., Zhang, H., Wu, H., Kong, W., et al. (2017b). Therapeutic efficacy of AAV8-mediated intrastriatal delivery of human cerebral dopamine neurotrophic factor in 6-OHDA-induced parkinsonian rat models with different disease progression. PLoS ONE *12*, e0179476.

Waspe, A.C., McErlain, D.D., Pitelka, V., Holdsworth, D.W., Lacefield, J.C., and Fenster, A. (2010). Integration and evaluation of a needle-positioning robot with volumetric microcomputed tomography image guidance for small animal stereotactic interventions. Med. Phys. *37*, 1647–1659.

Watabe-Uchida, M., Zhu, L., Ogawa, S.K., Vamanrao, A., and Uchida, N. (2012). Whole-brain mapping of direct inputs to midbrain dopamine neurons. Neuron *74*, 858–873.

Whishaw, I.Q., Cioe, J.D., Previsich, N., and Kolb, B. (1977). The variability of the interaural line vs the stability of bregma in rat stereotaxic surgery. Physiol. Behav. *19*, 719–722.

Whone, A.L., Boca, M., Luz, M., Woolley, M., Mooney, L., Dharia, S., Broadfoot, J., Cronin, D., Schroers, C., Barua, N.U., et al. (2019). Extended treatment with glial cell line-derived neurotrophic factor in Parkinson's disease. J. Parkinsons Dis. *9*, 301–313.

Wichmann, T., and Dostrovsky, J.O. (2011). Pathological basal ganglia activity in movement disorders. Neuroscience *198*, 232–244.

Wolak, D.J., and Thorne, R.G. (2013). Diffusion of macromolecules in the brain: implications for drug delivery. Mol. Pharm. *10*, 1492–1504.

Yona, G., Meitav, N., Kahn, I., and Shoham, S. (2016). Realistic numerical and analytical modeling of light scattering in brain tissue for optogenetic applications. eneuro *3*, ENEURO.0059-0015.2015.

Zaczek, R., Simonton, S., and Coyle, J.T. (1980). Local and distant neuronal degeneration following intrastriatal injection of kainic acid. J. Neuropathol. Exp. Neurol. *39*, 245–264.

Scouten, C.W., 2019. Stereotaxic Accuracy (Leica Biosystems). https://www.leicabiosystems.com/knowledge-pathway/stereotaxic-accuracy/.

STAR★METHODS

KEY RESOURCES TABLE

REAGENT or RESOURCE	SOURCE	IDENTIFIER
Antibodies		
mouse anti-GFAPx488 Alexafluor	Alexafluor	Cat: AB_194324
rabbit anti-NeuN	EMD Millipore	Cat: AB_177487
goat anti-Iba1	Abcam	Cat: AB_5076
Chemicals, Peptides, and Recombinant Proteins		
isoflurane	Patterson Veterinary	07-893-1389
C&B Metabond® Quick Adhesive Cement System	Parkell	SKU: S380
Ortho-Jet BCA Liquid	Lang Dental	Item #: B1303
Ethilon Suture 5-0 Nylon P-3 Undyed 18" Monofilament 12/Bx	Ethicon Inc,a J & J Company	6544169
Radioactive Cu-64	Mallinckrodt Institute of Radiology	N/A
Phosphate-Buffered Saline	Corning	Product Number 21-040-CV
Paraformaldehyde, 4% in PBS	Alfa Aesar	J61899-AK
Sucrose	Alfa Aesar	J64270-A1
Tissue-Tek® O.C.T. Compound	Sakura	4583
Hoechst 33342 Solution	ThermoFisher Scientific	62249
ProLong Gold Antifade Mountant	ThermoFisher Scientific	P10144
Experimental Models: Organisms/Strains		
Female Sprague Dawley rats	Charles River Laboratories	Crl:SD
Software and Algorithms		
VivoQuant	Invicro	N/A
MATLAB 2018a	Mathworks	N/A

RESOURCE AVAILABILITY

Lead Contact

Further information and requests for resources should be directed to and will be fulfilled by lead contact, Michael J. Cima (mjcima@mit.edu).

Materials Availability

This study did not generate new unique reagents.

Data and Code Availability

This study did not generate any unique datasets. Data and code developed and utilized in this study are available from the lead contact upon reasonable request.

EXPERIMENTAL MODELS AND SUBJECT DETAILS

Sprague Dawley female rats (8 weeks old, 200-250 g) were purchased from Charles River Laboratories and maintained under standard 12 hr light/dark cycles. All animal studies were approved by the Committee on Animal Care at the Massachusetts Institute of Technology.

METHOD DETAILS

COMMAND: Algorithm and computational approach

Three-dimensional representations of distinct brain structures were obtained from the 3D Brain Atlas Reconstructor (http://www.3dbar.org) which integrates several widely used stereotactic rat brain atlases (Calabrese et al., 2013; Paxinos, 2007). These models

represent the geometry of the brain structure by specifying the position and shape of polygons in three-dimensional space. We discretized these models via a finely spaced (~0.01 mm) grid for computational analysis.

An algorithm was developed to identify the optimal position and volume of localized drug boluses in order to best target the structure of interest. A total error function was defined for a particular target ($\mathcal{T}$) and dose ($\mathcal{D}$), as in Equation 2, as the weighted sum of two errors terms, E_1 and E_2.

$$E(\mathcal{T},\mathcal{D}) = E_1 + W * E_2 \quad (2)$$

The algorithm sought to minimize this error function by optimizing over the parameters of the dose which included the positions of each dose along with the amount of drug delivered. The first error term was designed to penalize the algorithm when the target structure was not sufficiently filled. Specifically, this error term represents the amount of additional drug needed to completely fill the target structure, as in Equation 3,

$$E_1 = \int_{\mathcal{V}} \max(C_{tx} - C(\mathcal{V}), 0) d\mathcal{V} \forall \mathcal{V} \in \mathcal{T} \quad (3)$$

where $\mathcal{V}$ indicates the volume that is within the target, C_{tx} corresponds to the minimum effective concentration (MEC) required for therapeutic benefit, and $C(\mathcal{V})$ indicates the spatial drug concentration distribution. The second error term was designed to penalize the algorithm when regions outside of the target structure received drug. Specifically, the error term represents the total amount of drug delivered outside of the target structure, as in Equation 4,

$$E_2 = \int_{\mathcal{V}} C(\mathcal{V}) d\mathcal{V} \forall \mathcal{V} \notin \mathcal{T} \quad (4)$$

where $\mathcal{V}$ indicates the volume that is not within the target. The weighting parameter (W) can be set by the user depending on the particular application and the relative tradeoff desired between minimizing the first versus the second error. The error function was computed numerically by first finely discretizing a three-dimensional volume containing the target structure and candidate drug boluses and then performing the requisite volume integrals. The optimization was performed using a standard iterative gradient descent algorithm. Execution was accelerated by exploring multiple convergence basins simultaneously through distributed computing.

A flowchart of COMMAND is shown in Figure S4, along with examples of stereotaxic coordinates used by prior studies in Figure S5 (Aoi et al., 2000; Bilang-Bleuel et al., 1997; Cederfjäll et al., 2015; Hattori et al., 1998; Horellou et al., 1994; Kilbourn et al., 1997; Kirik et al., 2000; Luo et al., 1999; Mandel et al., 1998; Rodrigues et al., 2003; Sacaan et al., 1991; Shults et al., 1996; Wang et al., 2017a, 2017b; Zaczek et al., 1980).

Optical simulation

Three-dimensional mouse brains structures were similarly obtained from the 3D Brain Atlas Reconstructor (http://www.3dbar.org) and discretized via a 3D grid for computational analysis. Monte Carlo simulations were implemented using the ScatterBrain application to simulate photon absorption and scattering in neural tissue for a variety of optical fibers (Yona et al., 2016). A similar algorithm was developed to identify the optimal fiber location and incident angle to maximize the volume of light in the target structure. The light profile was defined as all voxels containing greater than 1% of peak light intensity. The optimization was performed using iterative gradient descent and accelerated via distributed computing.

The optimization searches for the five parameters (x, y, z, ϕ_1, ϕ_2) for a flat-faced optical fiber to maximize on-target coverage. The coordinates x, y, and z denote the location of the tip of the fiber. The angles ϕ_1 and ϕ_2 define two angles of rotation, the first along the coronal plane and the second along the sagittal plane. The angles ϕ_1 and ϕ_2 are each allowed to vary on the interval $[-90^\circ, 90^\circ]$. The objective function did not include a term to minimize off-target leakage due to the fixed emission profile of each fiber. Each fiber was parameterized by its radius and numerical aperture, and its corresponding emission profile was calculated using an analytical beam spread function solver in neural tissue (scattering coefficient = 211 cm^{-1}, absorption coefficient = 0, anisotropy index = 0.86 g, refraction index = 1.36) as described previously (Yona et al., 2016). The light power is in arbitrary units as the light intensity is normalized to the max intensity occurring at the tip of the probe. The absolute power density will therefore be specific to a given experiment. The emission profiles shown in Figure S6 depict the isosurface corresponding to 1% of the max intensity of the entire emission spectra. All points within the isosurface are weighted equally in our objective function.

Characterizing brain structure irregularity

Three-dimensional representations of distinct brain structures were obtained from the 3D Brain Atlas Reconstructor (http://www.3dbar.org) (Paxinos, 2007). The compactness of each structure was defined as the ratio between the volume of the structure and the volume of a sphere with a surface area equivalent to that of the structure. The bounding volume and surface area for each structure was computed via Delaunay triangulation (Shewchuk, 2002). Increasing values of compactness indicate that the structure is more spherical (up to a maximum compactness of 1).

Device Fabrication

Infusion coordinates for optimal dosing of specific brain structures were output by the algorithm described above. Multi-cannula devices were fabricated according to these coordinates, with infusion points identical to those generated computationally. Devices were micromachined using a Cameron CNC micromachining center (Sonora, CA, USA). Infusion cannulas consisted of fused silica/polyimide tubing (inner diameter 15 μm, outer diameter 90 μm). Length of each cannula was tuned to vary resistance along each channel proportional to the desired flow through it. Theoretical fluidic resistance was calculated as

$$R = \frac{8\mu L}{\pi r^4}$$

Where R is fluid resistance, μ is the fluid viscosity, L is the length of the channel, and r is the channel radius.

Device implantation in rats

Sprague Dawley female rats were purchased from Charles River Laboratories and maintained under standard 12 hr light/dark cycles. All animal studies were approved by the Committee on Animal Care at the Massachusetts Institute of Technology. All materials used in surgeries were sterilized by autoclaving for 40 min at 120°C. Rats were anesthetized with isoflurane before having their heads shaven and disinfected with alternating betadine and 70% ethanol scrubs, three times each. Animals underwent bilateral craniotomy and had devices implanted over the left side of the cortex, and two ground screws implanted on the right hand side. The screw was placed such that the tip did not penetrate the brain. Briefly, the rats were placed in a stereotactic frame, and a midline incision was made to expose the skull. Burr holes were created using a dental drill and 0.5 mm drill bit. Devices and screws were then cemented to the skull using C&B Metabond adhesive (Parkell Inc., Edgewood NY) and Orthojet dental cement (Lange Dental, Wheeling, IL), and the incision was closed using 5-0 monofilament non-resorbable suture and 3M tissue glue. Custom made caps composed of 31G stainless steel connector coated with UV-cured epoxy were inserted into the protruding FEP tubing, to prevent dust and microbes form entering the tubing causing clogging and infection. Animals were noted to ambulatory and healthy 1-week post-op. Animals were used for PET infusion studies outlined below.

PET infusions, imaging, and reconstruction

Positron emission tomography (PET) was used to visualize dosing of radioactive tracer *in vivo*. Radioactive Cu-64 was obtained from the Mallinckrodt Institute of Radiology (St. Louis, MO) in the form of copper chloride, and diluted with saline to 3 mCi/mL activity concentration. Manufactured devices were inserted into agarose brain phantoms (0.6% w/v) embedded in plastic blocks (*in vitro*) or rodents as described above (*in vivo*). They were then connected with a syringe pump backfilled with radioactive Cu-64. Radioactive tracer solution was then infused intracerebrally (1.67 μL/min) via chronically implanted devices. For striatum targeting, a total of 2.6 and 3.1 μL, respectively, was infused through custom devices developed for two and three-bolus. All infusions were performed over 10 min. Immediately following infusion, the animal was imaged using a Perkin Elmer G8 PET/CT Preclinical Scanner. Three discrete infusions were performed for each of two and three bolus experiments. All infusions were imaged sequentially two or three times in 5-min intervals for a total n = 7 and n = 8 delivery profiles for, respectively, two and three bolus experiments. Images were reconstructed using MLEM 3D with 60 iterations. PET data were then analyzed *in Vivo*Quant Analysis software (inviCRO, LLC, MA, USA) by drawing a line profile through the maximum intensity profile of the bolus. Voxel dimensions of the PET image reconstruction were 0.457 × 0.457 × 0.457 mm^3.

Chronic *In Vivo* Biocompatibility Assessment

Two rats underwent device implantation as described above. At 2 months post-implantation, animals were euthanized using carbon dioxide asphyxiation. Each rat consequently underwent cardiac perfusion of 60 mL 1x phosphate buffered saline (PBS) solution (Corning Inc., Corning, NY), followed by 60 mL 4% paraformaldehyde (PFA) solution (Alfa Aesar, Ward Hill, MA). The head was then removed and immersed in 4% PFA for 48 hr. The implanted devices were extracted, and the brain removed and placed in 4% PFA overnight, and consequently in sinking solutions of increasing sucrose (Amresco Inc., Solon, OH) concentration (10%, 20% and 30%, overnight or until brain sinks).

Histology Protocol of Chronic *In Vivo* Biocompatibility

The brain was embedded in frozen tissue embedding medium (Sakura Finetek USA, Torrance, CA), and frozen in a liquid nitrogen bath. Transverse slices (20 mm) were cut using a Leica CM1900 cryostat (Leica Biosystems Inc., Buffalo Grove, USA), starting at the top of the brain, and descending 80 mm, past the tips of the previously implanted devices. Slides were stored at −80°C.

Slides were stained for astrocytes (glial fibrillary acidic protein (GFAP)), microglia (Iba1), neurons (NeuN), and nuclei (Hochst/DAPI), removed from −80°C, placed at room temperature for 20 min, and rehydrated by placing in a 1x PBS solution for 10 min. Samples were then immersed in blocking solution (5% Bovine serum albumin (BSA) (Rockland, Limerick, PA)) for 50 min, followed by overnight incubation at 4°C in primary antibody incubation solution. (1:100 mouse anti-GFAPx488 Alexafluor, 1:300 rabbit anti-NeuN, (EMD Millipore, Billerica, MA, USA), 1:300 goat anti-Iba1 (Abcam, Cambridge, MA) in incubation buffer (1% BSA, 1% normal Dk serum, 0.3% Triton X-100, 0.1% sodium azide).

Slides were rinsed 3 times in 1x PBS (0.1% Tween) and incubated in secondary antibody solution (1:300 Dk x Gt x Cy3 & 1:300 Dk x Rb x Dy650 (Abcam) for 40 min. Samples were rinsed 3 times in 1x PBS, and incubated with Hoechst solution (0.1 μg/ml) for 5 min, followed by mounting in gold antifade mounting medium (Life Technologies, Carlsbad, CA). Images were taken using fluorescence microscopy (EVOS FL Auto, Life Technologies, Grand Island, NY).

QUANTIFICATION AND STATISTICAL ANALYSIS

In Figure 5J, a description of the statistical tests and sample size is provided in the figure caption. Statistical analysis was performed using MATLAB 2018a (Mathworks, USA). Animals were randomized in their assignment to experimental groups. No samples were excluded from analysis.